Key Points:
- The type of step overs between ridge-transform fault segments is determined from the plate spreading rate and fault segment lengths
- A scaling relation for the critical step over length at which mantle flow starts to thin the lithosphere is derived
- Na_8.0 concentrations in dredged basalts follow the predicted trend based on the critical step over length

Supporting Information:
- Supporting Information S1

Correspondence to:
M. Wolfson-Schwehr,
monica.schwehr@gmail.com

Thermal segmentation of mid-ocean ridge-transform faults

Monica Wolfson-Schwehr[1,2] (ID), Margaret S. Boettcher[1,3] (ID), and Mark D. Behn[4] (ID)

[1]Department of Earth Sciences, University of New Hampshire, Durham, New Hampshire, USA, [2]Now at Monterey Bay Aquarium Research Institute, Moss Landing, California, USA, [3]Now at School of Earth and Environment, University of Western Australia, Perth, Western Australia, Australia, [4]Department of Geology and Geophysics, Woods Hole Oceanographic Institute, Woods Hole, Massachusetts, USA

Abstract 3-D finite element simulations are used to calculate thermal structures and mantle flow fields underlying mid-ocean ridge-transform faults (RTFs) composed of two fault segments separated by an orthogonal step over. Using fault lengths and slip rates, we derive an empirical scaling relation for the critical step over length ($\widetilde{L}_S$), which marks the transition from predominantly horizontal to predominantly vertical mantle flow at the base of the lithosphere under a step over. Using the ratio of step over length (L_S) to $\widetilde{L}_S$, we define three degrees of segmentation: first-degree, corresponding to type I step overs ($L_S/\widetilde{L}_S \geq 3$); second-degree, corresponding to type II step overs ($1 \leq L_S/\widetilde{L}_S < 3$); and third-degree, corresponding to type III step overs ($L_S/\widetilde{L}_S < 1$). In first-degree segmentation, thermal structures and mantle upwelling patterns under a step over are similar to those of mature ridges, where normal mid-ocean ridge basalts (MORBs) form. The seismogenic area under first-degree segmentation is characteristic of two, isolated faults. Second-degree segmentation creates pull-apart basins with subdued melt generation, and intratransform spreading centers with enriched MORBs. The seismogenic area of RTFs under second-degree segmentation is greater than that of two isolated faults, but less than that of an unsegmented RTF. Under third-degree segmentation, mantle flow is predominantly horizontal, resulting in little lithospheric thinning and little to no melt generation. The total seismogenic area under third-degree segmentation approaches that of an unsegmented RTF. Our scaling relations characterize the degree of segmentation due to step overs along transform faults and provide insight into RTF frictional processes, seismogenic behavior, and melt transport.

Plain Language Summary Mid-ocean ridge-transform faults (i.e., strike-slip faults that accommodate lateral motion associated with seafloor spreading) are typically viewed as geometrically simple structures, where a continuous fault is located between two spreading ridges. However, high-resolution seafloor mapping has shown that the structure of these fault systems is often quite complex. Mid-ocean ridge-transform faults may be composed of two or more individual fault strands separated by a step over. Using results of numerical simulations, we show that the form of the step over is expected to vary systematically from small extensional basins to active spreading ridge segments, depending on the length of the step over, the length of the adjacent fault segments, and the plate tectonic spreading rate. Additionally, our results suggest that the chemistry of mid-ocean ridge basalts produced at the step over is expected to change systematically with the step over length. This work shows that while the structure of transform faults can significantly affect the thermal structure of the region, it can readily be determined from regional plate tectonic parameters (fault lengths, step over length, and spreading rate). Furthermore, this work provides key insights into frictional processes, seismic behavior, and melt transport along oceanic transform plate boundary faults.

1. Introduction

Many processes and properties of mid-ocean ridge-transform faults (RTFs) strongly correlate with the underlying thermal structure, including melt migration and pooling [*Gregg et al.*, 2009; *Bai and Montesi*, 2015], seismic behavior [*Abercrombie and Ekström*, 2001; *Bird et al.*, 2002; *Boettcher and Jordan*, 2004; *Boettcher and McGuire*, 2009], frictional and mechanical properties [*Furlong et al.*, 2001; *Behn et al.*, 2007; *Roland et al.*, 2010], serpentinization rates [*Rüpke and Hasenclever*, 2017], and physical fault structure [*Gregg et al.*, 2006; *Wolfson-Schwehr*, 2015]. Earthquake focal depths [*Abercrombie and Ekström*, 2001; *Braunmiller and Nábělek*, 2008; *Craig et al.*, 2014] and laboratory friction studies [*Boettcher et al.*, 2007] suggest that the base of the

seismogenic zone along RTFs coincides with approximately the 600°C isotherm. The seismogenic area above the 600°C isotherm, A_T, can be approximated as $A_T = C_T L^{1.5} V^{-0.5}$ based on a half-space cooling model; where C_T is a constant $= 4.1 \times 10^{-4}$ m/s$^{(1/2)}$, L is fault length and V is slip rate [*Boettcher and Jordan*, 2004].

Many studies of fault mechanics on RTFs assume a simplified fault structure, in which a single, throughgoing transform fault connects two mid-ocean ridge spreading segments [e.g., *Boettcher and Jordan*, 2004]. Assumptions of simplified RTF structure further lead to assumptions that RTFs are magma poor, as conductive cooling from the adjacent cold, dense lithosphere inhibits melt production beneath the transform [*Fox and Gallo*, 1984; *Shen and Forsyth*, 1992; *Bai and Montesi*, 2015]. Large-scale and small-scale step overs, associated with intratransform spreading centers (ITSCs), extensional basins, and jogs in the fault trace, however, have been identified on many RTFs, including Blanco [*Embley and Wilson*, 1992], Siqueiros [*Fornari et al.*, 1989], Gofar [*McGuire et al.*, 2012], Discovery [*Wolfson-Schwehr et al.*, 2014], and Eltanin [*Sykes and Ekström*, 2012]. These step overs divide the fault system into two or more parallel to subparallel fault segments. A fault system comprising multiple fault segments is thought to reflect a smaller seismogenic area than a single fault of the same total fault length. Additionally, the presence of extensional step overs along a fault system may pool melt from across the transform domain [*Gregg et al.*, 2009], and fresh basalts have been sampled within ITSCs along several segmented fault systems, including Garrett [*Hékinian et al.*, 1995], Siqueiros [*Perfit et al.*, 1996], Quebrada, Discovery, and Gofar [*Pickle et al.*, 2009].

Physical segmentation of RTFs can occur in response to a change in the direction of plate motion that causes extension across the fault [*Pockalny et al.*, 1997; *Gregg et al.*, 2009; *Bai and Montesi*, 2015]. On faster slipping transform faults, where the lithosphere is thinner, warmer, and weaker, extension may cause the lithosphere to thin and tear, resulting in a leaky transform, where magma is extruded into the transform domain. Continued extension can lead to the focusing of passive mantle upwelling and the formation of an ITSC, where significant extension is accommodated by dike intrusion and magma is frequently erupted on the seafloor [*Searle*, 1983; *Pockalny et al.*, 1997]. Extensional forces may also result in pull-apart basins, in which extension is primarily accommodated through normal faulting and fresh volcanics are rarely observed (e.g., Gorda and Surveyor Depressions on the Blanco Transform Fault) [*Embley and Wilson*, 1992].

In this study, we investigate the relationship between the physical segmentation of RTFs and their thermal structure using a series of steady state, three-dimensional finite element simulations. Based on these thermal models, we develop a set of empirically derived scaling relations that use the fault segment lengths, step over length, and slip rate to estimate the seismogenic area (A_T) for segmented, unsegmented, and thermally decoupled fault systems. Our scaling relation for seismogenic area is dependent on the critical step over length, $\widetilde{L}_S$, which defines the length of the step over for which the underlying mantle flow field at the base of the lithosphere is predominantly vertical, and advective heating thins the lithosphere to produce either a pull-apart basin or an active intratransform spreading segment. The results of this work are used to determine the degree of thermal segmentation, and correspondingly, the type of step over, for any two RTF segments separated by an orthogonal step over. We also examine real-world examples of segmented RTF systems and compare the type of step over to the enrichment of the mid-ocean ridge basalts being extruded along the step over using available samples from the PetDB database (v. 2.9.1) [*Lehnert et al.*, 2000].

2. Model Setup

Model simulations were run using the finite element software COMSOL Multiphysics® (v. 4.2a). A simplified transform fault system is represented by two fault segments of lengths L_1 and L_2, separated by an orthogonal step over of length L_S (Figure 1 and Table 1). Seven pairs of fault segments (L_1 and L_2 pairs) are modeled with lengths ranging from 10 to 150 km. The length of the step over between the transform segments is varied between $L_S = 0$ km, representing a single, unsegmented fault of length L_T ($L_T = L_1 + L_2$), and $L_S = 30$ km. The transform-parallel extent of the model space is determined by the total transform fault length, L_T, plus an additional 50 km beyond the end of each transform segment (Figure 1). The width of the model space in the ridge parallel direction is defined by the length of the two ridge segments ($L_R = 50$ km) plus the length of the step over (L_S). All models have a vertical extent of 100 km.
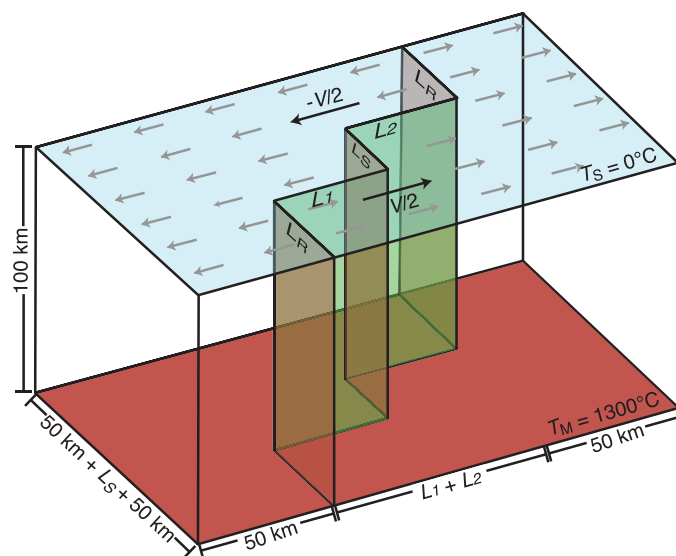
Figure 1. Model geometry for a segmented RTF system composed of two fault segments separated by an orthogonal step over. The transform fault segments have lengths L_1 and L_2, respectively. The step over has length L_S, and the ridge segments have length L_R, which is fixed at 50 km for all models. The length of the model space is determined by the total transform fault length ($L_1 + L_2$), plus an additional 50 km on either side of the ridge segments. The width of the model space is determined by the length of the two ridge segments ($2L_R = 100$ km) plus the length of the step over (L_S). All models have a vertical extent of 100 km.

Mantle flow is driven kinematically by imposing a half-spreading rate ($V/2$) on either side of the fault along the surface of the model for $V = 2$–14 cm/yr. Boundary conditions on the sides of the model parallel to the transform fault are symmetric, while those parallel to the ridges are stress free. The base of the model is also stress free, allowing convective flux into and out of the model domain without drag from the underlying mantle. The imposed temperature at the surface of the model, T_S, which represents the seafloor/seawater interface, is set to 0°C, and the base of the model is fixed to have a mantle potential temperature, T_M, of 1300°C. The surface of the model domain is meshed using a free-triangular grid with a variable element size that decreases toward the transform segments and the ridge axes. The surface mesh is then extruded vertically through the model domain, creating a network of prismatic elements with finer spacing at shallower depths. The node spacing is 1 km along the RTF and the adjacent ridge segments for fault geometries with a total fault length $L_T \leq 150$ km. For RTF geometries with $L_T > 150$ km, the node spacing is 2 km. The node-spacing is 1 km along step overs ≥ 5 km, and varied such that there are four equally spaced elements along step overs < 5 km in length. Vertically, the node spacing is 1 km for the shallowest 10 km below the surface; 2 km for depths between 10 and 20 km, 5 km for depths between 20 and 30 km, 10 km for depths between 30 and 50 km, and 25 km for depths between 50 and 100 km.

To derive the RTF temperature structure, we solve for conservation of mass, momentum, and energy, in steady state assuming the mantle behaves as an incompressible fluid. Solutions to the model are found using COMSOL's nonlinear stationary solver with the relative tolerance between iterative solutions is set to 1×10^{-6}. Following *Roland et al.* [2010], we impose a nonlinear temperature-dependent rheology with a viscoplastic approximation in the lithosphere. While this approach neglects elastic bending stresses in the lithosphere, the plastic failure criteria limit stress accumulation in the shallow lithosphere, and thus this simplification likely has a relatively minor influence on the underlying mantle flow structure (and its resulting influence on the thermal regime along the RTF).

Roland et al. [2010] showed that including enhanced hydrothermal circulation in the model can significantly cool the predicted fault thermal structure (e.g., the depth to the 600°C isotherm may deepen by a factor of up to 1.5 depending on model parameters). To preserve computational efficiency in our models, we do not include hydrothermal circulation. This simplification will influence the absolute temperatures in the shallow crust; however, it is unlikely to change the trends we observe in fault thermal structure with step over geometry. *Roland et al.* [2010] also looked at frictional weakening along the fault in

Table 1. Geometries of the Modeled Faults

Model Geometry	Length of Fault Segment 1 L_1 (km)	Length of Fault Segment 2 L_2 (km)	Total Fault Length $(L_1 + L_2)$ L_T (km)
1	50	50	100
2	10	90	100
3	25	75	100
4	40	60	100
5	100	100	200
6	80	120	200
7	50	100	150
Step over length, L_S (km)	0, 1, 2, 5, 10, 15, 20, 25, 30		

the form of serpentinization, which lowers the coefficient of friction from 0.85 to 0.1. Despite the significant reduction in friction along the fault, the changes in the thermal structure were negligible (1% reduction in A_T for a 100 km long fault slipping at 3 cm/yr). Because the goal of our study is to isolate the effect of step over geometry on RTF thermal structure, here we hold the coefficient of friction constant and neglect the effects of hydrothermal cooling.

Brittle deformation is approximated by computing the maximum shear stress, τ_{max}, as a function of the coefficient of friction, μ, the density of the lithosphere, ρ, the density of seawater, ρ_w, gravitational acceleration, g, depth, z, and cohesion, C:

$$\tau_{max} = \mu(\rho - \rho_w)gz + C \tag{1}$$

Equation (1) assumes that the maximum compressive principle stress, σ_1, is vertical, which is expected for mid-ocean ridge environments that are undergoing extension. For simplicity, this assumption is applied throughout the model domain, although we acknowledge that along the transform fault plane the vertical stress is expected to be the intermediate principle stress. Assuming σ_1 is vertical near the transform allows the fault to fail at slightly lower differential stresses than theoretically predicted; however, *Roland et al.* [2010] showed that this discrepancy has a negligible effect on the resulting flow field and temperature structure.

Following *Chen and Morgan* [1990], we calculate an effective viscosity for the lithosphere, η_{fric}, that is limited by τ_{max} and the second invariant of the strain rate tensor, $\dot{\varepsilon}_{II}$:

$$\eta_{fric} = \frac{\tau_{max}}{\sqrt{2}\dot{\varepsilon}_{II}} \tag{2}$$

Dislocation creep in the upper mantle is described by a temperature-dependent, non-Newtonian power law [*Kirby*, 1983]:

$$\dot{\varepsilon} = A(\sigma_1 - \sigma_3)^n \exp\left(-\frac{E}{RT}\right) \tag{3}$$

where $\dot{\varepsilon}$ is the uniaxial strain rate, $(\sigma_1 - \sigma_3)$ is the differential stress, and R is the gas constant. The values of A, the preexponential factor, n, the stress exponent, and E, the activation energy used in the model are obtained from experiments on dry olivine [*Hirth and Kohlstedt*, 2003; for values see Table 1]. The flow law is incorporated into our model by means of a creep viscosity that is a function of temperature and strain rate [*Chen and Morgan*, 1990]:

$$\eta_{creep} = \frac{1}{4}\left(\frac{4}{3A}\right)^{1/n} \dot{\varepsilon}_{II}^{\frac{1-n}{n}} \exp\left(\frac{E}{nRT}\right) \tag{4}$$

At each node in the model domain, deformation is dominated by the mechanism with the lowest viscosity. An effective viscosity is computed and used in the conservation of momentum equation to determine the flow field:

$$\eta_{eff} = \left(\frac{1}{\eta_{fric}} + \frac{1}{\eta_{creep}} + \frac{1}{\eta_{max}}\right)^{-1} \tag{5}$$

Table 2. Material Properties and Boundary Conditions for RTF Model Simulations

Material Properties		
ρ_{lith}	Average lithospheric density	3300 kg/m^3
ρ_w	Water density	1000 km/m^3
η_0	Reference viscosity	1×10^{19} Pa·s
η_{max}	Maximum viscosity	1×10^{24} Pa·s
k	Thermal conductivity	3 W/(m K)
C_p	Specific heat	1000 J/(kg K)
R	Gas constant	8.3145 J/(mol K)
A	Preexponential factor	1.1×10^5 MPa^{-n} s^{-1}
n	Stress exponent	3.5
E	Activation energy	520 kJ/mol
μ	Coefficient of friction	0.85
C	cohesion	20 MPa
g	Gravitation acceleration	-9.8 m/s^2
Boundary Conditions		
L_R	Length of ridge segment	50 km
V	Full spreading rate	2–14 cm/yr
T_S	Surface temperature	0°C
T_M	Mantle potential temperature	1300°C

The initial model run is computed using a constant viscosity term ($\eta_0 = 10^{19}$ Pa·s), and the resulting strain rate is used to compute the viscosity in equations (2) and (4). The effective viscosity (equation (5)) is then computed and used in the flow laws of the subsequent solutions. The maximum viscosity term in equation (5) is iteratively increased from η_0 to 10^{24} Pa·s and is included to prohibit unrealistically high stresses from building within the model and to aide in convergence.

The temperature in the model is computed using the heat equation, derived from Fourier's law of heat conduction and the conservation of energy, and assuming steady state flow:

$$\rho C_p u \cdot \nabla T = \nabla \cdot (k \nabla T) + Q \tag{6}$$

where ρ is density of the medium, C_p is the specific heat, u is the velocity field of the fluid, ∇T is the temperature gradient, k is the thermal conductivity, and Q are the heat sources.

3. Results

We start by considering a 100 km long RTF composed of two adjacent fault segments ($L_1 = 25$ km, $L_2 = 75$ km, $L_T = 100$ km) with a slip rate of 8 cm/yr. Figure 2a shows the thermal structure for a single, unbroken fault of length L_T. Figures 2b and 2c show segmented fault systems, where the 25 km long fault segment is separated from the 75 km long fault segment by a 2 km ($L_S = 2$ km) and 15 km ($L_S = 15$ km) step over, respectively. The thermal structure of the fault system with a 2 km long step over (Figure 2b) is
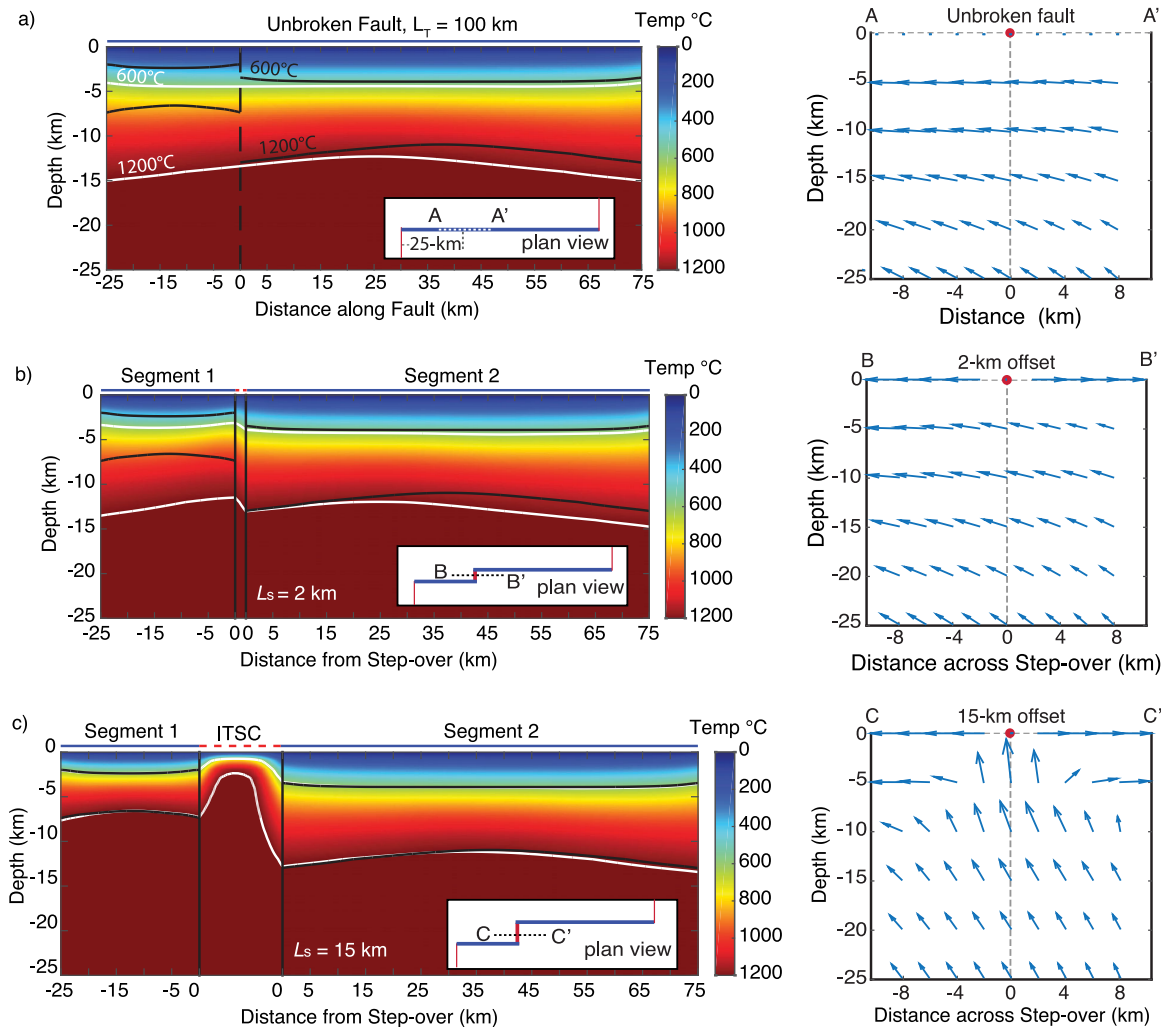

Figure 2. Temperature and mantle flow profiles for a RTF system. (a) A single, 100 km unsegmented RTF. The vertical dashed line marks the point (25 km along fault) where the step over will be included in (b) and (c). (b, c) Segmented fault systems comprised of one 25 km long fault segment and one 75 km long fault segment, with a 2 km long step over and 15 km long step over, respectively. Full spreading rate is 8 cm/yr in all cases. For plotting purposes, the step over, which is perpendicular to the fault segments, has been projected into the same plane as the faults along the profiles. Top and bottom white lines denote the 600 and 1200°C isotherms, respectively. The top and bottom black lines denote the 600 and 1200°C isotherms calculated independently for two single, unbroken RTFs; one with a length of 25 km, to represent segment 1, and the one with a length of 75 km to represent segment 2. All isotherms are labeled in Figure 2a. As the white isotherms approach the black ones, the two fault segments become increasing decoupled. Mantle flow calculated along a profile perpendicular to the step over are shown at right for each of the three geometries (see inset for location). The cross sections are oriented across the center of the step over and extend for 10 km on either side. Length of the arrows represents the relative flow velocity.

Table 3. Scaling Relation Variables

A_T	Area above the 600°C isotherm
A_U	The seismogenic area for an unsegmented RTF (equation (7))
A_S	The seismogenic area for one fault segment in a segmented fault system (equation (8))
L_x	The length of the fault segment being computed in A_S, either L_1 or L_2
A_{L_x}	Seismogenic area for a standalone fault segment of length L_x
A_D	Combined seismogenic area for two isolated faults of length L_1 and L_2 (equation (9))
A_G	The grouped A_T for two fault segments adjacent to the step over on a segmented RTF (equation (10))
$\widetilde{L_S}$	Critical step over length (equation (11))
R_A	Area loss ratio comparing the combined A_T for an RTF with and without a step over (equation (12))
R_D	Ratio comparing the depth to 1200°C isotherm under a step over to the depth under a mature spreading ridge (equation (13))
C_{600}	Scaling constant for A_T in equation (6), 6.9×10^{-4} m/s$^{(1/2)}$
C_0	Scaling constant for the critical step over length in equation (10), 1.4×10^{-4} m$^{1.1}$ s$^{-0.6}$
D_S	Depth of the 1200°C isotherm beneath the step over
D_R	Depth of the 1200°C isotherm beneath the ridge segment a distance sufficient to be outside the influence of the transform effect
D_{L_1}	Depth of the 1200°C isotherm under an unsegmented fault of length L_T at a distance L_1 from the ridge-transform intersection

very similar to that of the unsegmented fault (Figure 2a), with a reduction in seismogenic area (A_T) of only 8%. The isotherms underlying the 2 km step over (Figure 2b) deepen toward the 75 km long fault, but the thermal structure beneath the step over shows very little thinning of the lithosphere relative to the two adjacent transform fault segments. By contrast, the isotherms underneath the 15 km step over are significantly shallower than those underlying either of the two adjacent fault segments (Figure 2c). Further, the mantle flow field underlying the 15 km step over (Figure 2c) shows a significant component of vertical upwelling compared to the 2 km step over. The reduction in A_T between the unsegmented fault and the segmented fault system with the 15 km step over is 22%. The 600°C isotherm (top white line in Figure 2c) for the segmented fault system with a 15 km step over is nearly indistinguishable from that of thermal models computed for two isolated faults (e.g., a single unsegmented transform) of length 25 and 75 km, respectively (black lines). Thus, for this transform configuration ($L_1 = 25$ km, $L_2 = 75$ km, $V = 8$ cm/yr, and $L_S = 15$ km), the two adjacent fault segments are nearly thermally decoupled.

The seismogenic area of a single, unsegmented fault, increases with fault length, and decreases with spreading rate. As shown by *Behn et al.* [2007] and *Roland et al.* [2010], calculations with a viscoplastic rheology result in a different shape of the seismogenic area compared with that predicted by the half-space cooling model but yield a similar prediction for the total seismogenic area. As such, the area above the 600°C isotherm derived from our finite element models for a single, unsegmented fault, A_U, can be approximated by an empirically derived scaling relation:

$$A_U = C_{600} L_T^{1.5} V^{-0.5} \qquad (7)$$

where $C_{600} = 6.9 \times 10^{-4}$ (m/s)$^{(1/2)}$ (Table 3). The positive exponent on L_T in equation (7) can be attributed to an increase in conductive cooling with increasing distance from the ridge. The inverse relationship with square-root of slip rate, V, is related to advective heat loss due to the convective flux of the mantle and diffusive cooling from above. Faster spreading rates result in a warmer temperature profile and a lithosphere that is thinner and weaker. The empirically determined exponents on L and V in equation (7) are consistent with the theoretical values found in the scaling relation for seismogenic area (A_T) derived from the half-space cooling model (see supporting information) [*Boettcher and Jordan*, 2004].

For segmented fault systems, the seismogenic area of a fault segment adjacent to a step over, A_S, can be found from the empirically derived scaling relation:

$$A_S = A_U \left(\frac{L_X}{L_T}\right) \exp\left(\frac{-L_S}{\widetilde{L_S}}\right) + A_{L_x} \left[1 - \exp\left(\frac{-L_S}{\widetilde{L_S}}\right)\right] \qquad (8)$$

where L_X is the length of the fault segment (either L_1 or L_2 in Figure 1), and A_{L_x} is the seismogenic area for single, unbroken fault of length L_X (equation (7)). When the step over is small ($L_S/\widetilde{L_S} \rightarrow 0$) A_S reduces to $A_U(L_X/L_T)$, which is equivalent to the area of an unbroken fault of length L_T multiplied by the ratio of L_X to L_T. When $L_S \gg \widetilde{L_S}$, A_S approaches A_{L_x} (Figures 3a and 3c).

We define A_G as the grouped seismogenic area for the two fault segments adjacent to a step over (Table 3). The two adjacent fault segments are considered thermally decoupled if the step over length is sufficiently
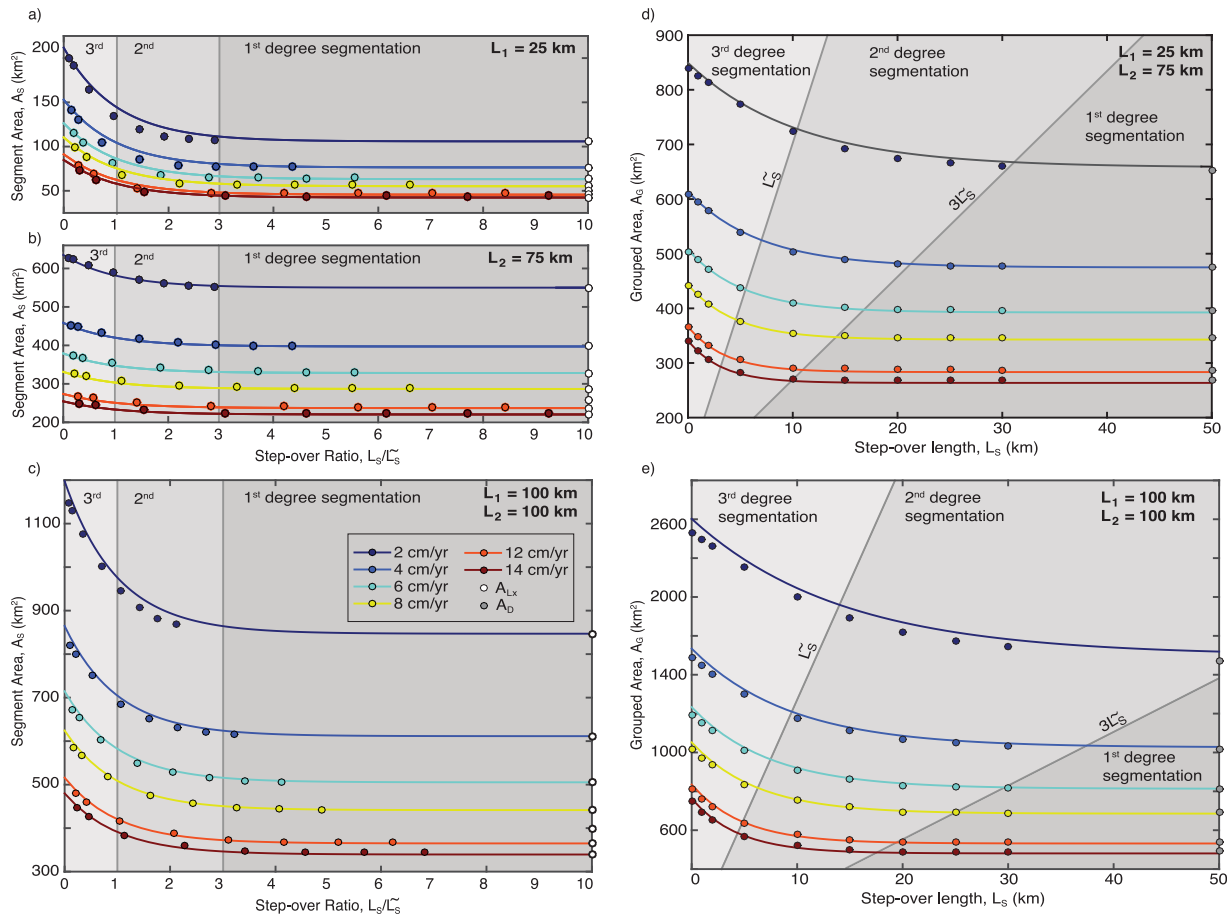
Figure 3. (a, b) The segment area, A_S, versus step over ratio, $L_S/\widetilde{L_S}$, for a segmented RTF system composed of a 25 km (Figure 3a) and a 75 km long fault segment (Figure 3b) for a range of the modeled slip rates. The scaling relation for A_S calculated from equation (8) (colored lines) can be directly compared with values of A_S derived from the model simulations (colored circles). Note that as the step over ratio increases, A_S approaches the area for a single fault, A_{Lx} as calculated from equation (7) (white circles). (c) A_S versus $L_S/\widetilde{L_S}$ for a segmented RTF system composed of two 100 km long fault segments. Since $L_1 = L_2$, only one plot is shown. (d) A_G versus L_S for the same fault geometry in Figure 3a. The scaling relation for A_G calculated from equation (10) (colored lines) can be compared with values of A_G derived from the model simulations (colored circles). As the step over length increases, A_G approaches A_D (equation (9); gray circles). (e) A_G versus L_S for the same fault geometry in Figure 3c. In each plot, the gray scale backgrounds denote the degrees of segmentation based on $L_S/\widetilde{L_S}$ and are labeled accordingly on the figures.

large such that any additional increase in L_S produces a negligible change in A_G (Figures 3b and 3d). In this case, the "decoupled" seismogenic area is simply equal to the sum of A_T for two independent faults of length L_1 and L_2, and is given as

$$A_D = C_{600}\left(L_1^{1.5} + L_2^{1.5}\right)V^{-0.5} \tag{9}$$

A_G can then be expressed in terms of A_U and A_D:

$$A_G = A_U \exp\left(\frac{-L_S}{\widetilde{L_S}}\right) + A_D\left[1 - \exp\left(\frac{-L_S}{\widetilde{L_S}}\right)\right] \tag{10}$$

where the critical step over length, $\widetilde{L_S}$, is empirically derived (equation (11)) and represents the step over length for which the underlying flow field produces sufficient vertical flow to thin the lithosphere and promote decompression melting. When the step over is small and the step over ratio ($L_S/\widetilde{L_S}$) approaches 0, A_G approaches A_U. For longer step overs where $L_S \gg \widetilde{L_S}$, the step over ratio increases and A_G approaches A_D. The critical step over length, $\widetilde{L_S}$, is based on L_1, L_2, and V, such that

$$\widetilde{L_S} = C_O \frac{L_1^{1.5} + L_2^{1.5} - 0.1|L_1 - L_2|^{1.5}}{L_1 + L_2} V^{-0.6} \tag{11}$$

where $C_O = 1.4 \times 10^{-4}$ m$^{1.1}$ s$^{-0.6}$. The term $0.1|L_1 - L_2|^{1.5}$ aides in the fit of the scaling relation for fault geometries where L_2 is $\gg L_1$. The decrease in the exponent on the slip rate, V, in comparison to the one

used for the seismogenic area scalings (–0.6 versus −0.5), provides a significantly better fit at slower slip rates (see supporting information). Removing the $0.1|L_1-L_2|^{1.5}$ term increases the maximum percent error by 8%, while increasing the exponent on V to -0.5 increases the maximum percent error by 15%. These differences are likely related to the influence of the viscoplastic rheology on the resulting fault thermal structure.

By substituting $(L_1/L_T)L_T$ and $(L_2/L_T)L_T$ for L_1 and L_2, respectively, equation (9) can also be used to compute the percentage of area loss between A_D for a decoupled segmented fault system and A_U for the unbroken fault. In the case of the fault geometry in Figure 2, where $L_1 = 25$ km and $L_2 = 75$ km, we find $(L_1/L_T)L_T = (1/4)L_T$ and $(L_2/L_T)L_T = (3/4)L_T$. Plugging these values into equation (9) and simplifying gives $(0.77)C_{600}L_T^{1.5}V^{-0.5}$, indicating that there is a ∼23% area loss between a fully decoupled and an unsegmented RTF. Thus, we can see that fault geometry modeled in Figure 2c, with a step over length of 15 km and a computed area loss of 22%, is very close to being completely decoupled.

To compare transform thermal structure across all modeled geometries and slip rates, we define a seismogenic area loss ratio:

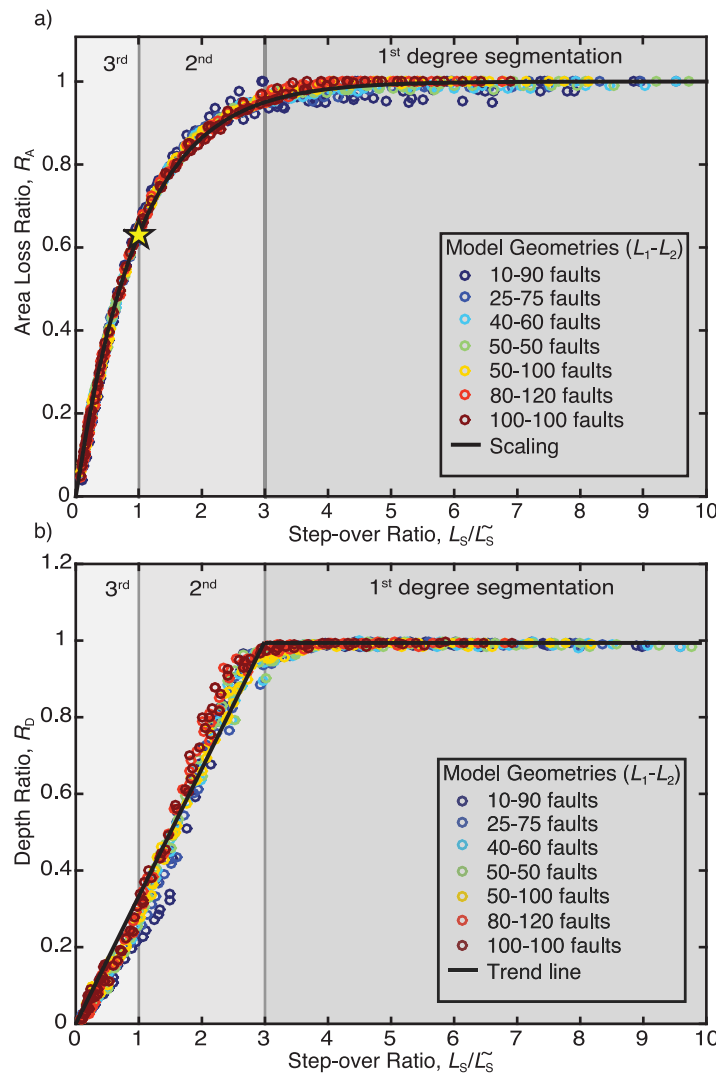$$R_A = \frac{A_U - A_G}{A_U - A_D} \quad (12)$$

such that for very long step overs $R_A \cong 1$, and as the step over length approaches 0, R_A approaches 0 (Figure 4a and Table 3). Substituting equation (10) into equation (12), gives $R_A = 1 - \exp(-L_S/\widetilde{L}_S)$ and shows that for $L_S/\widetilde{L}_S = 1$, $R_A \approx 0.63$. Full decoupling of the two adjacent fault segments occurs when an increase in L_S results in a negligable decrease in A_G ($R_A \approx 1$, $L_S/\widetilde{L}_S > 3$).

Our model results were also used to examine changes in mantle flow and the thickness of the lithosphere beneath the step over. Along a mature ridge segment, mantle flow under the ridge axis is primarily vertical throughout the upper mantle, leading to decompression melting and the creation of new oceanic crust. The base of the thermal lithosphere, where melting terminates beneath a mature ridge segment, can be approximated by the depth of the 1200°C isotherm. Comparing the depth of the 1200°C isotherm beneath the step over (D_S) to that beneath the adjacent 50 km long ridge segments (D_R) provides a quantitative estimate of the degree, or maturity, of the RTF segmentation. The depth of the 1200°C isotherm

Figure 4. (a) Seismogenic area loss ratio, R_A, versus the step over ratio, $L_S/\widetilde{L}_S$ for all modeled geometries at all slip rates. Seismogenic area calculated from the model runs (colored circles) can be compared with the scaling relation for R_A (black curve) computed using equation (12), and based on equations (7) and (9)–(11). The star indicates where $L_S/\widetilde{L}_S = 1$ and corresponds to $RA = 0.63$. (b) Ratio of the depth to the 1200°C isotherm, R_D, versus the step over ratio, $L_S/\widetilde{L}_S$. Colored circles represent depth ratios computed directly from the model according to equation (13). The solid line shows the trend of the data.

underneath the ridge segment is taken from our models at a sufficient distance away from the ridge-transform intersection to be outside the influence of the "transform edge effect," wherein the ridge thermal structure is cooled due to the adjacent cold, dense lithosphere on the other side of the fault.

To compare results across the range of model geometries and slip rates, we define a ratio of depths to the 1200°C isotherm, or a lithospheric thinning ratio, R_D, based on D_S at the center of the step over:

$$R_D = \frac{D_S - D_{L_1}}{D_R - D_{L_1}} \tag{13}$$

where D_{L_1} is the depth of the 1200°C isotherm under an unsegmented fault of length L_T at a distance L_1 from the ridge-transform intersection (e.g., if $L_1 = 25$ km and $L_2 = 75$ km, D_{L_1} is the depth of the 1200°C isotherm underneath a 100 km long unsegmented fault at a distance of 25 km from the RTI; the bottom white isotherm in Figure 2a). When L_S is $\ll \widetilde{L_S}$, $D_S \approx D_{L_1}$ and R_D is ~ 0. As $L_S / \widetilde{L_S}$ approaches 3, D_S approaches D_R, and R_D approaches 1 (Figure 4b).

For the segmented fault systems shown in Figure 2, we calculate $\widetilde{L_S} = 4.4$ km (from equation (11)). The step over ratios for $L_S = 2$ km (Figure 2b) and 15 km (Figure 2c), are therefore 0.45 and 3.4, respectively. When $L_S / \widetilde{L_S} = 0.45$, $R_A \approx 0.4$ (see Figure 4b), indicating that step over lengths less than $\widetilde{L_S}$ still influence the thermal structure of the adjacent fault segments, although the lithosphere is not thinned sufficiently to form a mature spreading segment (Figure 2b). However, when $L_S / \widetilde{L_S} = 3.4$, $R_A \approx 0.97$, corresponding to nearly complete thermal decoupling of the two adjacent fault segments (Figure 2c). The flow field underneath the 15 km long step over is predominately vertical up to the surface (Figure 2c), and the depth of the 1200°C isotherm under the step over is within ~ 3 km of the seafloor, indicating that the thermal structure beneath the step over approximates that of a mature ridge segment.

The relationship between A_S and L_S, as well as A_G and L_S, are shown in Figure 3 for two sample geometries (the 25–75 km segment geometry as shown in Figure 2, and the 100–100 km segment geometry). In all plots, the lines represent values computed from our scaling rations (equation (8) for A_S and equation (10) for A_G) and the circles denote values computed directly from the models. The closeness in fit shows how well the scaling relations perform. Both A_S and A_G exponentially decrease as L_S increases, with the most significant decrease occurring when L_S is less than $\widetilde{L_S}$. As L_S approaches $3\widetilde{L_S}$, the rate of decrease tapers off. For $L_S \ll \widetilde{L_S}$, A_G is approximately equivalent to A_U, and A_S is approximately equal to $(L_X/L_T) \times A_U$ (where L_X is either L_1 or L_2). For $L_S > 3\widetilde{L_S}$, A_G approaches A_D, and A_S approaches A_{L_X}. The slower the fault slip rate, the more gradual the decrease in A_G and A_S.

4. Discussion

The critical step over length, $\widetilde{L_S}$, which is determined from the length of the transform segments and the fault slip rate, provides the primary constraint on the thermal state of a segmented oceanic transform fault. It can be used to compute: (1) the total seismogenic area of a segmented RTF and (2) the degree of thermal influence between the adjacent fault segments. Using $\widetilde{L_S}$, we define three degrees of segmentation for RTFs: first-degree segmentation, where $L_S / \widetilde{L_S} \geq 3$; second-degree segmentation, where $1 \leq L_S / \widetilde{L_S} < 3$, and third-degree segmentation, where $L_S / \widetilde{L_S} < 1$ (Figure 5).

For first-degree segmentation (Figure 5a), which corresponds to a type I step over ($L_S / \widetilde{L_S} \geq 3$), the upwelling rate underlying the center of the step over is approximately the same as that underlying a mature ridge segment and we define these step overs as ITSCs. In the upper asthenosphere, mantle flow along a type I step over or ITSC is predominantly vertical, while near the base of the lithosphere, mantle flow is focused toward the center of the ITSC (Figure 5, A–A'). Furthermore, the depth to the 1200°C isotherm under the center of a type I step over is within $\sim 5\%$ of the depth to the 1200°C isotherm underneath a mature ridge, indicating that the step over behaves like a typical ridge segment. Type 1 step overs result in a reduction in seismogenic area of $\geq 23\%$ between the segmented fault system and an unbroken fault with the same total length. As the length of the step over increases from $3\widetilde{L_S}$ to $4\widetilde{L_S}$, The seismogenic area of the segmented fault system continues to decrease as R_A approaches 1. Beyond $4\widetilde{L_S}$, any increase in the length of the step over has only a negligible effect on the thermal structure and seismogenic area of the adjacent faults, and the two fault segments are considered fully thermally decoupled.
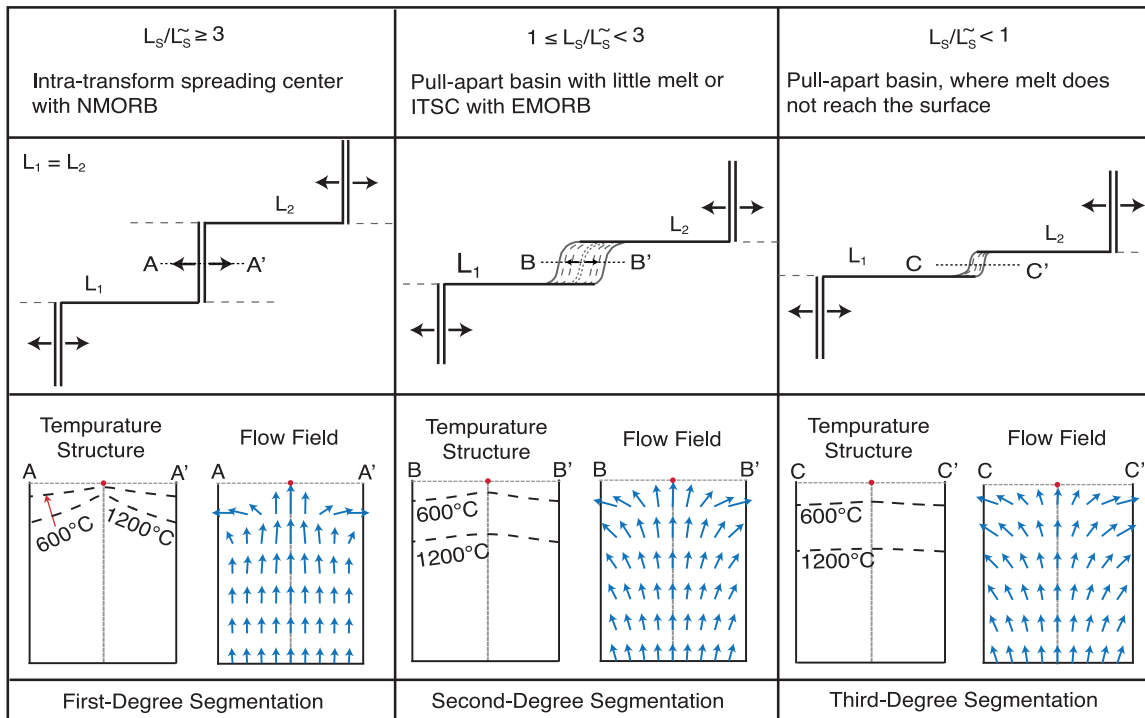
Figure 5. Cartoon sketch showing plan view and cross-sectional views of the structure of transform fault step overs expected under the three degrees of thermal segmentation: first-degree segmentation, which corresponds to a type I step over ($L_S/\widetilde{L_S} \geq 3$); second-degree segmentation, which corresponds to a type II step over ($1 \leq L_S/\widetilde{L_S} < 3$); and third-degree segmentation, which corresponds to a type III step over ($L_S/\widetilde{L_S} < 1$). The two adjacent transform fault segments are illustrated schematically to be the same length. In the plan view (second row), black arrows indicate direction of seafloor spreading, while straight dashed lines represent inactive fracture zones. In the third row, the 600 and 1200°C isotherms, as well as the mantle flow velocities, are plotted across the center of the step over, extending 10 km on either side and from the surface of the seafloor down to a depth of 30 km. The red dot and vertical dashed line in the center of the flow field plots represents the location of the step over.

In second-degree segmentation (type II step overs, $1 \leq L_S/\widetilde{L_S} < 3$; Figure 5b), the lithosphere is thinned, facilitating melting and possible eruption along the step over, but the thinning is not as extreme in type I step overs. As $L_S/\widetilde{L_S}$ approaches 1, the mantle flow at the base of the lithosphere beneath the step over becomes progressively dominated by horizontal flow with a decreasing component of upwelling. Thus, the magma budget for the step over likely decreases as $L_S/\widetilde{L_S}$ decreases. The lithosphere beneath the step over is thin relative to an unbroken transform, indicating that these step overs could significantly affect the mechanical and frictional properties of the fault system. The reduction in the seismogenic area can be significant (∼14–22%) between the segmented fault system with a type II step over and an unbroken fault with the same total fault length.

For third-degree segmentation (type III step overs, $L_S/\widetilde{L_S} < 1$; Figure 5c), the perturbation in the thermal structure is sufficiently small that the seismogenic area of the segmented fault system is comparable to that of an unbroken RTF and there is little lithospheric thinning beneath the step over. Consequently, these step overs are best described as pull-apart basins, with little melt generation or transport to the surface. Any melt that is present along the step over has likely migrated into the transform domain from the adjacent spreading ridges [*Bai and Montesi*, 2015]. Flow on either side of the step over is directed primarily horizontally into the adjacent lithosphere (Figure 5, C–C') and the thermal structure of a type III step over is similar to that of the adjacent fault segments with little shoaling of the isotherms. However, type III step overs should not be discounted as unimportant features along transform faults. While the width of the seismogenic zone along the step over is sufficient to allow for possible earthquake propagation from one fault segment to the next, small (sub-km) step overs have been found at the termination of repeating earthquake rupture patches on a few RTFs [*McGuire et al.*, 2012; *Wolfson-Schwehr et al.*, 2014]. The seismic velocity structure of these small step overs are best explained as regions with significant porosity [*Roland et al.*, 2012; *Froment et al.*, 2014], which likely affects the fault composition [*Rüpke and Hasenclever*, 2017] as well as the fault frictional properties, thereby providing a control on rupture propagation.

Well-documented observations suggest that the empirically derived relationship between $\widetilde{L_S}$ and the type of step over holds for real-world segmented RTF systems. On the Blanco Transform Fault, for example, the western end of the 135 km long Blanco Ridge fault segment is terminated by the ~17 km long Cascadia Depression. The fault segments on either side of Blanco Ridge are both ~41 km long, and the mean slip rate of the Blanco Transform Fault system is ~5.1 cm/yr (GSRM v1.2) [*Kreemer et al.*, 2003], corresponding to $\widetilde{L_S}$ of ~8 km. The Cascadia Depression, therefore, is defined by $L_S/\widetilde{L_S} = \sim 2$, consistent with a type II step over, where melt has the potential to reach the surface. Indeed, the Cascadia Depression is interpreted to be an ITSC based on the presence of a narrow ridge within the depression that is flanked by a series symmetrically spaced inwardly facing back-tilted fault blocks [*Embley and Wilson*, 1992] and acoustic opaque zones in seismic reflection profiles suggesting igneous intrusions [*Dziak et al.*, 2000]. To the east, Blanco Ridge ends in the ~8 km long Gorda Depression, which corresponds to $L_S/\widetilde{L_S} = \sim 1$, and is interpreted to be an extensional basin based on morphological similarities to mature pull-apart basins found on continental divergent wrench faults [*Embley and Wilson*, 1992].

To investigate whether there are systematic variations in melt chemistry with type of step over, we compiled a data set from the PetDB database (v. 2.9.1) [*Lehnert et al.*, 2000] of glass and whole rock analyses taken from samples dredged from the ITSCs along a number of RTFs. While rare earth element concentrations are not reported for many of the samples, they all have MgO and Na_2O concentration. Following *Klein and Langmuir* [2003], we compute $Na_{8.0}$ concentrations (Na_2O concentration normalized to a MgO content of 8 wt %) from the MgO and Na_2O concentrations, using the relation $Na_{8.0} = Na_2O + 0.373(MgO) - 2.98$. We then use the $Na_{8.0}$ concentrations as a proxy for melt enrichment, following the works of *Langmuir and Forsyth* [2007] and *Gregg et al.* [2009]. Na is a magmaphile element, being incompatible within the crystals that remaining in the solid mantle during melting, and its concentration is inversely proportional to the extent of melting [*Langmuir and Forsyth*, 2007]. Thus, as melting commences, Na preferentially accumulates in the melt, leaving the remaining solid mantle depleted in Na. Mid-ocean ridge basalts (MORBs) formed from this early stage of melting are considered enriched (EMORB) as they contain higher concentrations of magmaphile elements. As the extent of the melting column increases, the concentration of Na will decrease due to the addition of low Na melts that dilute the initial enriched melt. This type of MORB becomes depleted with respect to magmaphile elements and is typically referred to as normal MORB (NMORB). Thus, we expect type I step overs, which have a similar thermal structure and mantle flow field to that of mature ridge segments, to have NMORB, while type II step overs, where the magma budget is likely reduced, to have more EMORB. Type III step overs, which show little change in thermal structure compared with that of an unsegmented fault, are predicted to have little to no melt production, thus we do not expect to find many type III samples in our data set.

Figure 6 shows a map of the step overs compiled from PetDB (Figure 6a) and computed $Na_{8.0}$ concentrations versus $L_S/\widetilde{L_S}$ (Figure 6b). Step overs are named for the fault they are on and the segments they connect; e.g., Raitt_AB is a step over on the Raitt Transform Fault that connects fault segment A to fault segment B, where fault segments are lettered from east to west. The trend of the data shows more enriched MORB at type II step overs and NMORB at type I step overs, in agreement with our predictions above. The lack of basalts collected from type III step overs in the PetDB database is consistent with our prediction of little to no melt production, while the more enriched MORB found along type II step overs and NMORB found along type I is consistent with an increasing melt supply with greater lithospheric thinning and higher melt production.

There are two step overs that stand out as anomalous in Figure 6: Quebrada_CD and Guamblin_Darwin. Quebrada_CD, has a mean $Na_{8.0}$ concentration of 2.55 wt %, which is low compared to other type II step overs and suggests a more depleted melt. There are three additional ITSCs on Quebrada, but none have samples in the PetDB database. In the case of the Guamblin-Darwin fault, the $Na_{8.0}$ concentration is high compared to other type III step overs, suggesting a more enriched magma with a lower extent of melting. Future work is necessary to better understand the cause of these anomalies.

The Quebrada, Discovery, and Gofar Transform Faults are three individual transform fault systems collectively known as QDG, located at ~4°S on the East Pacific Rise. Each of these transform faults is segmented into two or more fault strands, separated by what are interpreted to be small ITSCs on the basis of their morphology and the presence of young magmas with relatively high MgO concentrations recovered from dredged basalts within the step overs [*Pickle et al.*, 2009]. The high MgO concentrations within the ITSC
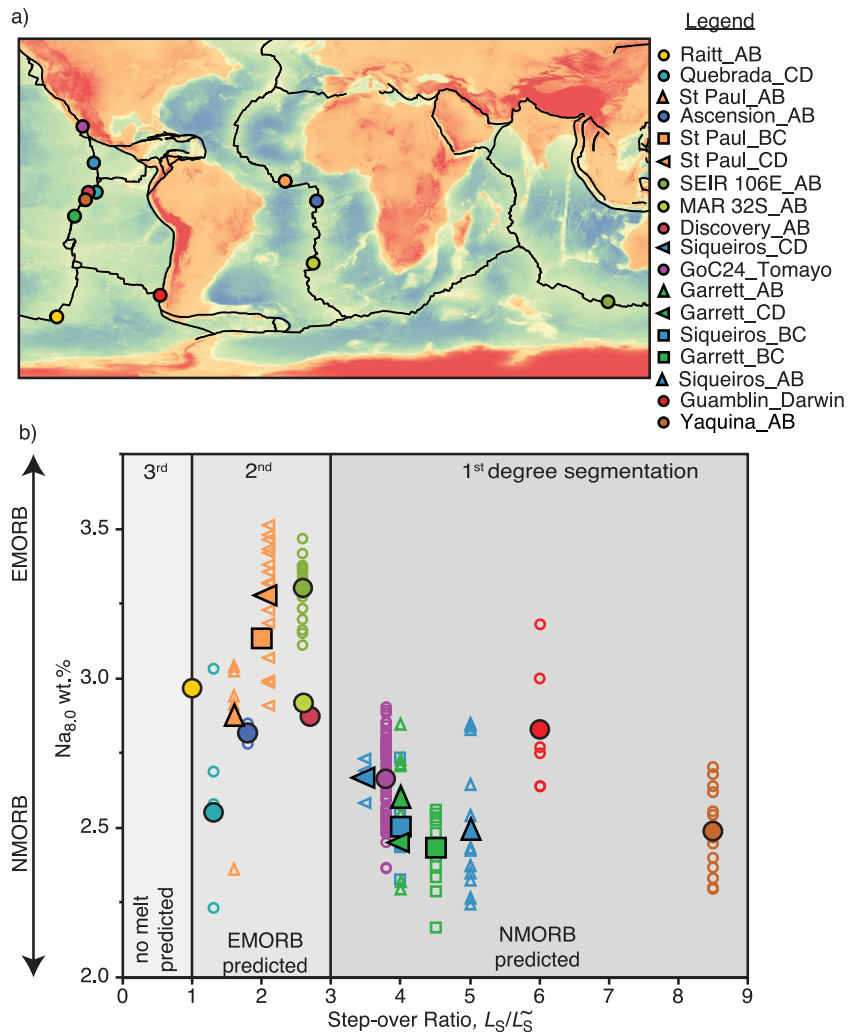
Figure 6. (a) Map of the fault locations with step overs plotted in (b). Colors of the location circles in the map correspond to the colors in the legend. (b) Na$_{8.0}$ wt % (Na$_2$O concentration normalized to 8 wt % MgO) versus step over ratio, $L_S/\widetilde{L_S}$, for a number of segmented RTFs across the global mid-ocean ridge system. Open symbols represent individual samples obtained from the PetDB database, while filled symbols indicate the average for each step over. Symbols in the legend are in order of increasing step over ratio, with the same color, but different shapes, given to step overs in an individual RTF. For step overs with only one sample, there is a filled symbol plotted. Na$_{8.0}$ indicates enriched MORB produced from smaller degrees of melting associated with shorter ITSCs and less pronounced mantle upwelling. Lower Na$_{8.0}$ values are associated with greater extents of melting, which produce more depleted normal MORB.

basalts indicate more primitive melts that have undergone less differentiation. The step overs along QDG produce third-degree segmentation ($L_S/\widetilde{L_S} \geq 3$), with the two exceptions of the 4 km ITSC on Quebrada ($L_S/\widetilde{L_S} = 1.3$) and the 8 km long step over on Discovery ($L_S/\widetilde{L_S} = 2.7$). These type II step overs are the only ITSCs on QDG to have samples in the PetDB database (Quebrada_CD and Discovery_AB, respectively). The estimated crustal thicknesses of the ITSCs are all between 5 and 7 km [*Pickle et al.*, 2009], representing full oceanic crustal thickness. ITSCs appear able to pool melts from across the transform domain, as opposed to being limited to the width of the ridge [*Gregg et al.*, 2009], so it may be possible to generate full crustal thickness along type II step overs with geochemically enriched melts.

5. Conclusions

In this study, we used three-dimensional finite element simulations to model the thermal structure underlying a segmented mid-ocean ridge-transform fault system, in which two adjacent transform fault segments are separated by an orthogonal step over. A scaling relation for the critical step over length, $\widetilde{L_S}$, was derived from the tectonic parameters of fault length and slip rate. The critical step over length is the length of step

over under which the plate divergence across the step over generates sufficient vertical upwelling to generate substantial thinning of the lithosphere. We use $\widetilde{L}_S$ to define the degree of thermal coupling between adjacent fault segments, as well as the grouped seismogenic area of the segmented fault system. The critical step over length is also used to define three degrees of RTF segmentation based on thermal structure and the mantle flow field. First-degree segmentation characterizes type I step overs, $L_S \geq 3\widetilde{L}_S$, where the depth to the 1200°C isotherm beneath the step over is within 5% of the depth to the 1200°C isotherm underneath a mature ridge segment, and the grouped seismogenic area of the RTF approaches the combined seismogenic area of two distinct faults. Second-degree segmentation corresponds to type II step overs, $\widetilde{L}_S \leq L_S < 3\widetilde{L}_S$, where vertical mantle flow is sufficient to cause lithospheric thinning, and the seismogenic area of the adjacent fault segments are strongly influenced by one another. Third-degree segmentation pertains to type III step overs, $L_S < \widetilde{L}_S$, where mantle flow under the step over is predominantly horizontal at the base of the lithosphere, there is little lithosphere thinning, and the grouped seismogenic of the RTF approaches that of an unbroken fault system. The decrease in $Na_{8.0}$ concentrations from dredged basalts from step overs along segmented transform faults with increasing step over ratio is consistent with the predicted increase in melt supply and greater lithospheric thinning.

The scaling relation for the critical offset length provides a means to determine the type of step over separating any two transform fault segments, from pull-apart basins with little to no melt production and immature ITSCs with enriched MORB, to mature ITSCs with normal MORB that are comparable to mature ridge segments. In addition, the scaling relations for seismogenic area of segmented RTFs can be used to provide insight into frictional processes, seismogenic behavior, and melt transport along RTFs.

References

Abercrombie, R. E., and G. Ekström (2001), Earthquake slip on oceanic transform faults, *Nature*, *410*(6824), 74–77, doi:10.1038/35065064.

Bai, H., and L. G. J. Montesi (2015), Slip-rate-dependent melt extraction at oceanic transform faults, *Geochem. Geophys. Geosyst.*, *16*, 401–419, doi:10.1002/2014GC005579.

Behn, M. D., M. S. Boettcher, and G. Hirth (2007), Thermal structure of oceanic transform faults, *Geology*, *35*(4), 307–310, doi:10.1130/G23112A.1.

Bird, P., Y. Y. Kagan, and D. D. Jackson (2002), Plate tectonics and earthquake potential of spreading ridges and oceanic transform faults, in *Plate Boundary Zones*, edited by S. Stein and J. T. Freymueller, pp. 203–218, AGU, Washington, D. C.

Boettcher, M. S., and T. H. Jordan (2004), Earthquake scaling relations for mid-ocean ridge transform faults, *J. Geophys. Res.*, *109*, B12302, doi:10.1029/2004JB003110.

Boettcher, M. S., and J. J. McGuire (2009), Scaling relations for seismic cycles on mid-ocean ridge transform faults, *Geophys. Res. Lett.*, *36*, L21301, doi:10.1029/2009GL040115.

Boettcher, M. S., G. Hirth, and B. Evans (2007), Olivine friction at the base of oceanic seismogenic zones, *J. Geophys. Res.*, *112*, B01205, doi:10.1029/2006JB004301.

Braunmiller, J., and J. Nábělek (2008), Segmentation of the Blanco Transform Fault Zone from earthquake analysis: Complex tectonics of an oceanic transform fault, *J. Geophys. Res.*, *113*, B07108, doi:10.1029/2007JB005213.

Chen, Y., and W. J. Morgan (1990), A nonlinear rheology model for mid-ocean ridge axis topography, *J. Geophys. Res.*, *95*(B11), 17,583–17,604, doi:10.1029/JB095iB11p17583.

Craig, T. J., A. Copley, and J. Jackson (2014), A reassessment of outer-rise seismicity and its implications for the mechanics of oceanic lithosphere, *Geophys. J. Int.*, *197*(1), 63–89, doi:10.1093/gji/ggu013.

Dziak, R. P., C. G. Fox, R. W. Embley, J. L. Nabelek, J. Braunmiller, and R. A. Koski (2000), Recent tectonics of the Blanco Ridge, eastern blanco transform fault zone, *Mar. Geophys. Res.*, *21*(5), 423–450, doi:10.1023/A:1026545910893.

Embley, R. W., and D. S. Wilson (1992), Morphology of the Blanco Transform Fault Zone-NE Pacific: Implications for its tectonic evolution, *Mar. Geophys. Res.*, *14*(1), 25–45, doi:10.1007/BF01674064.

Fornari, D. J., D. G. Gallo, M. H. Edwards, J. A. Madsen, M. R. Perfit, and A. N. Shor (1989), Structure and topography of the Siqueiros transform fault system: Evidence for the development of intra-transform spreading centers, *Mar. Geophys. Res.*, *11*(4), 263–299, doi:10.1007/BF00282579.

Fox, P. J., and D. G. Gallo (1984), A tectonic model for ridge-transform-ridge plate boundaries: Implications for the structure of oceanic lithosphere, *Tectonophysics*, *104*(3–4), 205–242.

Froment, B., J. J. McGuire, R. D. Hilst, P. Gouédard, E. C. Roland, H. Zhang, and J. A. Collins (2014), Imaging along-strike variations in mechanical properties of the Gofar transform fault, East Pacific Rise, *J. Geophys. Res. Solid Earth*, *119*, 7175–7194, doi:10.1002/2014JB011270.

Furlong, K. P., S. D. Sheaffer, and R. Malservisi (2001), Thermal-rheological controls on deformation within oceanic transforms, *Geol. Soc. Spec. Publ.*, *186*(1), 65–83, doi:10.1144/GSL.SP.2001.186.01.05.

Gregg, P. M., J. Lin, and D. K. Smith (2006), Segmentation of transform systems on the East Pacific Rise: Implications for earthquake processes at fast-slipping oceanic transform faults, *Geology*, *34*(4), 289, doi:10.1130/G22212.1.

Gregg, P. M., M. D. Behn, J. Lin, and T. L. Grove (2009), Melt generation, crystallization, and extraction beneath segmented oceanic transform faults, *J. Geophys. Res.*, *114*, B11102, doi:10.1029/2008JB006100.

Hékinian, R., D. Bideau, R. Hebert, and Y. Niu (1995), Magmatism in the Garrett transform fault (East Pacific Rise near 13°27'S), *J. Geophys. Res.*, *100*(B6), 10,163–10,185, doi:10.1029/94JB02125.

Hirth, G., and D. L. Kohlstedt (2003), Rheology of the upper mantle and the mantle wedge: A view from the experimentalists, in *Inside the Subduction Factory, Geophysical Monograph*, vol. 138, pp. 83–105, AGU, Washington, D.C., doi:10.1029/138GM06.

Kirby, S. H. (1983), Rheology of the lithosphere, *Rev. Geophys.*, *21*(6), 1458, doi:10.1029/rg021i006p01458.

Klein, E. M., and C. Langmuir (1987), Global Correlations of Ocean Ridge Basalt Chemistry with Axial Depth and Crustal Thickness, *J. Geophys. Res.*, *92*(B8), 8089–8115, doi:10.1093/petrology/egm051.

Kreemer, C., W. E. Holt, and A. J. Haines (2003), An integrated global model of present-day plate motions and plate boundary deformation, *Geophys. J. Int.*, *154*(1), 8–34, doi:10.1046/j.1365-246X.2003.01917.x.

Langmuir, C., and D. Forsyth (2007), Mantle melting beneath mid-ocean ridges, *Oceanography*, *20*(1), 78–89, doi:10.5670/oceanog.2007.82.

Lehnert, K., Y. Su, C. H. Langmuir, B. Sarbas, and U. Nohl (2000), A global geochemical database structure for rocks, *Geochem. Geophys. Geosyst.*, *1*(5), 1012, doi:10.1029/1999GC000026.

McGuire, J. J., J. A. Collins, P. Gouédard, E. C. Roland, D. Lizarralde, M. S. Boettcher, M. D. Behn, and R. D. van der Hilst (2012), Variations in earthquake rupture properties along the Gofar transform fault, East Pacific Rise, *Nat. Geosci.*, *5*(5), 336–341, doi:10.1038/ngeo1454.

Perfit, M., et al. (1996), Recent volcanism in the Siqueiros transform fault: Picritic basalts and implications for MORB magma genesis, *Earth Planet. Sci. Lett.*, *141*(1–4), 91–108.

Pickle, R. C., D. W. Forsyth, N. Harmon, A. N. Nagle, and A. Saal (2009), Thermo-mechanical control of axial topography of intra-transform spreading centers, *Earth Planet. Sci. Lett.*, *284*(3–4), 343–351, doi:10.1016/j.epsl.2009.05.004.

Pockalny, R. A., P. J. Fox, D. J. Fornari, K. C. Macdonald, and M. R. Perfit (1997), Tectonic reconstruction of the Clipperton and Siqueiros Fracture Zones: Evidence and consequences of plate motion change for the last 3 Myr, *J. Geophys. Res.*, *102*(B2), 3167–3181, doi:10.1029/96JB03391.

Roland, E. C., M. D. Behn, and G. Hirth (2010), Thermal-mechanical behavior of oceanic transform faults: Implications for the spatial distribution of seismicity, *Geochem. Geophys. Geosyst.*, *11*, Q07001, doi:10.1029/2010GC003034.

Roland, E. C., D. Lizarralde, J. J. McGuire, and J. A. Collins (2012), Seismic velocity constraints on the material properties that control earthquake behavior at the Quebrada-Discovery-Gofar transform faults, East Pacific Rise, *J. Geophys. Res.*, *117*, B11102, doi:10.1029/2012JB009422.

Rüpke, L. H., and J. Hasenclever (2017), Global rates of mantle serpentinization and H_2 production at oceanic transform faults in 3-D geodynamic models, *Geophys. Res. Lett.*, *44*, 6726–6734, doi:10.1002/2017GL072893.

Searle, R. C. (1983), Multiple, closely spaced transform faults in fast-slipping fracture zones, *Geology*, *11*(10), 607, doi:10.1130/0091-7613(1983)11 < 607:MCSTFI>2.0.CO;2.

Shen, Y., and D. W. Forsyth (1992), The effects of temperature-and pressure-dependent viscosity on three-dimensional passive flow of the mantle beneath a ridge-transform system, *J. Geophys. Res.*, *97*(B13), 19,717.

Sykes, L. R., and G. Ekström (2012), Earthquakes along Eltanin transform system, SE Pacific Ocean: Fault segments characterized by strong and poor seismic coupling and implications for long-term earthquake prediction, *Geophys. J. Int.*, *188*(2), 421–434, doi:10.1111/j.1365-246X.2011.05284.x.

Wolfson-Schwehr, M. (2015), The relationship between oceanic transform fault segmentation, seismicity, and thermal structure, PhD thesis, Univ. of N. H., Durham.

Wolfson-Schwehr, M., M. S. Boettcher, J. J. McGuire, and J. A. Collins (2014), The relationship between seismicity and fault structure on the Discovery transform fault, East Pacific Rise, *Geochem. Geophys. Geosyst.*, *15*, 3698–3712, doi:10.1002/2014GC005445.